Journal of the Mechanics and Physics of Solids 137 (2020) 103868

Contents lists available at ScienceDirect

Journal of the Mechanics and Physics of Solids

journal homepage: www.elsevier.com/locate/jmps

Discrete element models of fracture in tooth enamel: Failure mode competition and statistical effects

J. William Pro[a], Francois Barthelat[a,b,*]

[a] Department of Mechanical Engineering, McGill University, 817 Sherbrooke Street West, Montreal, QC H3A 2K6, Canada
[b] Department of Mechanical Engineering, University of Colorado, 427 UCB, 1111 Engineering Dr, Boulder, CO 80309, United States

ARTICLE INFO

Article history:
Received 12 October 2019
Revised 19 December 2019
Accepted 8 January 2020
Available online 10 January 2020

Keywords:
Discrete element modeling
Enamel
Fracture mechanics
Decussation
Cross-ply
Statistical fracture

ABSTRACT

Capturing how cracks initiate and propagate in tooth enamel is difficult because of the complex three-dimensional microstructure of this material. In this work we use the discrete element method (DEM) to model fracture in idealized enamel structures where the enamel rod microstructure is explicitly represented with DEM elements. The model captures the interactions of a propagating crack with the mineral rods and their interfaces, including crack deflection and penetration into the rods. We used this model to assess the effect of relative strength and stiffness between the rods and the interfaces, of the decussation angle, and of statistical distributions of defects in the mineral rods. We show that higher strength rods (smaller flaws) promote interface crack deflection and branching which increases toughness through spreading of an inelastic region. Stiffer rods increase the load carried by the rod, which ultimately decreases crack resistance. Statistical variations in rod strength were shown to have an overall negative impact on the average crack resistance. In particular, for high coefficients of variation we observed substantial nucleation of 'daughter' cracks far from the main crack, which steer the main crack along the weakest trajectories and decrease overall toughness. This model and results provide insights to better interpret fracture experiments in human or bovine enamel, as well as better guidelines for the design of synthetic dental and bioinspired materials.

1. Introduction

Enamel is a complex bioceramic with a microstructure consisting of crisscrossing (decussating) mineral rods bonded by proteins and mineral bridges (Pro and Barthelat, 2019). The three-dimensional morphology of enamel is relatively complex, but its function is straightforward: to provide reliable and efficient mastication, which implies three requirements in terms of mechanical properties: hardness, stiffness, and resistance to fracture. While these properties are mutually exclusive in engineered materials (Ashby and Cebon, 1993), natural composites overcome this limitation and show remarkable combinations of mechanical properties from billions of years of evolution of their microarchitecture. Enamel is an example of a material with extreme hardness (it is the hardest material in the human body) which combines relatively high toughness. Tightly packed and parallel mineral rods generate hardness and stiffness at the surface (Jiang et al., 2005; Cuy et al., 2002; Park et al., 2008), while toughness is generated by trapping cracks into regions of mineral rod decussation

* Corresponding author at: Department of Mechanical Engineering, University of Colorado, 427 UCB, 1111 Engineering Dr, Boulder, CO 80309, United States.
E-mail address: francois.barthelat@colorado.edu (F. Barthelat).

https://doi.org/10.1016/j.jmps.2020.103868
0022-5096/

(Yahyazadehfar and Arola, 2015; Bajaj and Arola, 2009a; Yahyazadehfar et al., 2013). In contrast, engineered hard ceramic coatings suffer from brittleness (Evans et al., 2001), which limits their reliability and lifespan.

Recently, conventional fracture mechanics experiments have directly shown that decussating enamel exhibits rising crack resistance (R-curve) behavior in both humans (Yahyazadehfar and Arola, 2015; Bajaj and Arola, 2009a; Yahyazadehfar et al., 2013; Bajaj and Arola, 2009b) and bovines (Bechtle et al., 2010). As in many composites (e.g., fibrous woven composites (Rajan and Zok, 2014), multilayered ceramic coatings (Evans et al., 2001), etc.), the toughening micromechanisms in enamel are complex and involve progressive and interacting failure between the hard and soft phases. A wide array of fracture mechanisms in including crack bridging, interface deflection, branching, and direct fracture in the hard phase (e.g., fracture of 'bundles' of rods) has been observed in enamel and correlated with fracture toughness (Bajaj and Arola, 2009a; Yahyazadehfar et al., 2013; Bajaj and Arola, 2009b; Bechtle et al., 2010). Failure is further complicated by nondeterministic fracture of the mineral phase due to statistical distributions in flaws and defects, a well-known phenomenon for many brittle materials (Lu et al., 2002). Indeed experimental R-curves can show significant scatter and variability (Yahyazadehfar and Arola, 2015), which is likely due to statistical variations of structures and properties across different teeth and even within the same tooth.

While many experiments have begun to elucidate the fracture mechanisms in enamel, there are very few numerical models of crack propagation because of the complexity of enamel failure. In particular there are no models that explicitly model the competition between crack propagation along an interface (between the rods) and penetration into the hard phase itself (through the rods), where the latter is governed by defect distributions and Weibull type statistics. This is a substantial lack as global enamel failure involves complex combinations of both types of failure as observed in almost all fracture mechanics based experiments in enamel to date. Extended finite element models (XFEM) have captured crack propagation in enamel but they relied on homogenization of the microstructure (Barani et al., 2012), and therefore did not explicitly capture relationships between microstructure and crack resistance. Phase field models have captured some interacting fracture mechanisms in nacre and Bouligand structures but have yet to be applied in numerical simulations of enamel (Yin et al., 2019; Khandelwal et al., 2017). In our previous study (Pro and Barthelat, 2019) we modeled elasticity, hardness, crack propagation, and toughness in enamel with discrete element modeling (DEM). This numerical method is computationally efficient, so that the complex enamel microarchitecture can be represented explicitly in large fracture models (Pro and Barthelat, 2019). These DEM models successfully captured rising R-curves along with the associated failure modes and sources of toughness. However, these models were based on an implicit approach and often faced convergence difficulties when simulating rod fracture. In addition these models only considered perfectly periodic enamel-like architectures with no statistics. In general the effect of statistical variations in microstructure on the mechanics of biological composites is less understood, but it can be significant. Our previous models of nacre-like materials in uniaxial tension have shown that statistics on average have a negative impact on modulus, strength, and energy absorption which can be partially offset by strain hardening (Pro et al., 2015a; Abid et al., 2019). Other computational fracture models have considered the effects of statistics on crack propagation in ductile materials with explicit random inclusions (Srivastava et al., 2014; Needleman and Tvergaard, 1991); yet there still remains a lack of statistics-based models of crack propagation in complex composites including enamel.

The object of this work is therefore threefold: (i) to develop a robust explicit DEM-based computational approach that can handle complex fracture mechanisms without convergence issues, (ii) to capture the competition between rod fracture and interface fracture during crack propagation and (iii) to assess the effect of statistical distributions of flaws within the enamel rods. This work builds upon our previous study but provides new connections between the effect of rod to interface strength contrast and statistical flaw distributions, in particular the effect of 'weak patches' ahead of the dominant flaw that influence its trajectory and overall toughness. We first outline the numerical approach and subsequently study the effect of decussation, rod-to-interface strength contrast, and stiffness mismatch. Lastly we use the method to model the effect of flaws which are manifested through spatial statistical variations in rod strength.

2. Enamel fracture model and computational approach

Fig. 1a shows a schematic of the idealized 3D enamel microarchitecture and its corresponding discrete element model (DEM). The geometrical model is identical to that used in our previous study (Pro and Barthelat, 2019), but here brittle rod fracture including statistics is considered, and the numerical solutions were obtained using an explicit time stepping algorithm (instead of the implicit approach we used previously). The enamel architecture is assumed to be a crossply where the plies are stacked in the z-direction, with each successive ply consisting of rods that alternate in relative orientation from one ply to the next. The 3D architecture is completely defined by two independent geometrical parameters (Fig. 1b): the average rod diameter d, defined as the perpendicular distance between the centerlines of two adjacent intraply rods, and the decussation angle θ_D, which indicates the orientation of the rods relative to the (vertical) x-axis. Note that this definition of the decussation angle differs from the convention used in dental biology (Cox, 2013) by a factor of two but for consistency we have kept the same definition as used in our previous work (Pro and Barthelat, 2019). Fig. 1b highlights the discretization and connectivity of the DEM model, showing three different projection views in both the vertical (xy) and horizontal (yz) planes. The horizontal view slices are denoted with labels 1–3, and vertical view slices are denoted with labels 4–6 and are indicated on both Fig. 1a and 1b for clarity. The rods are modelled as beams discretized by beam elements and nodes, and nodes from adjacent rods also interact via interface elements. Fig. 1b (column 2) shows how the interfaces are connected through the depth of the enamel geometry: at each discrete layer in the yz-plane, the interfaces

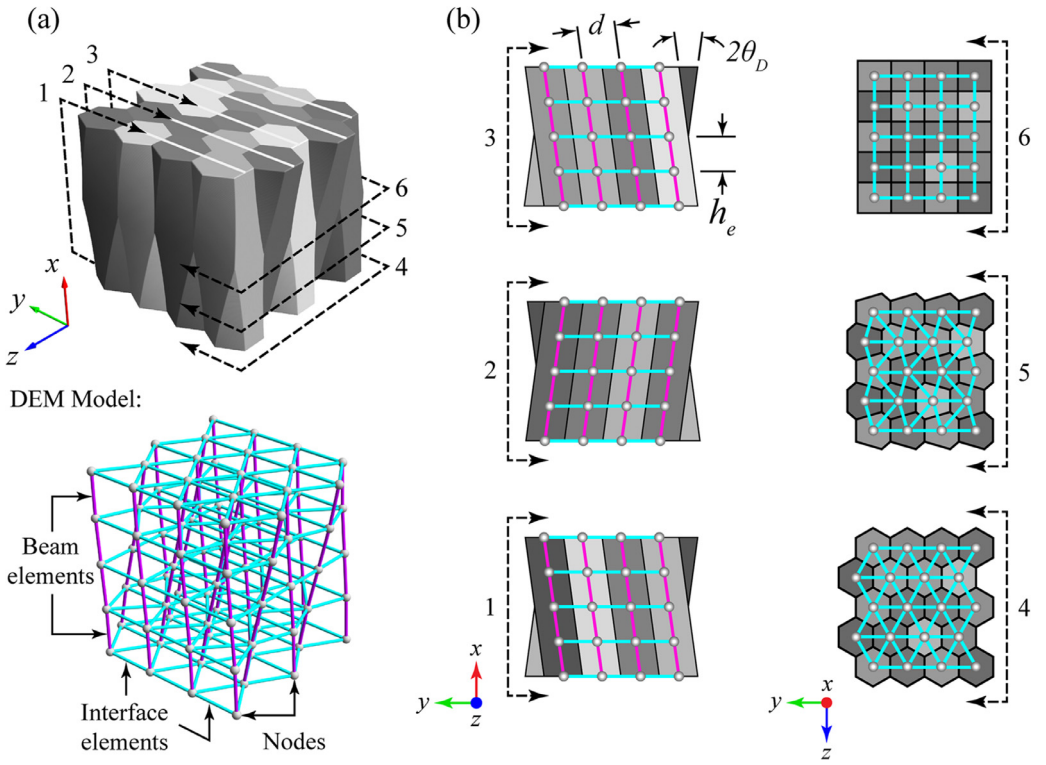

Fig. 1. Different views of the 3D enamel model. (a) Idealized enamel architecture with 3D DEM model of beam and interface elements. (b) DEM model and connectivity superposed on the idealized architecture different horizontal and vertical cross sections. Note that each rod is rendered with a slightly different grayscale coloring simply for illustrative purposes to distinguish the rod boundaries.

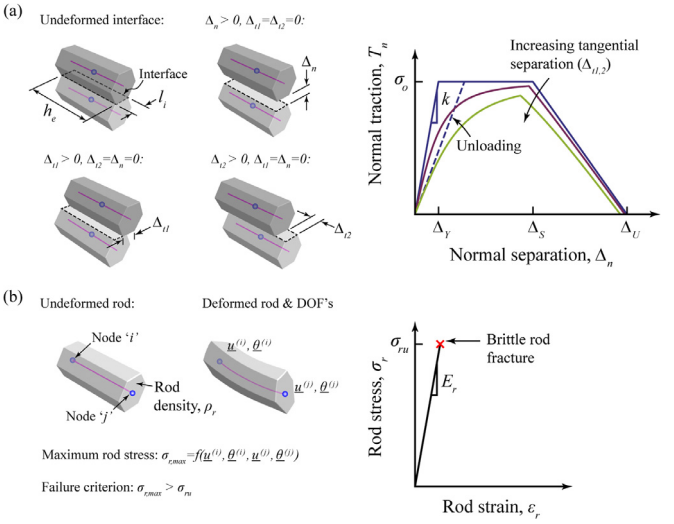

Fig. 2. Deformation modes and constitutive material model for (a) the interfaces and (b) the rods.

follow exactly the nearest-neighbor connectivity of the corresponding Voronoi contour as in Pro and Barthelat (2019). For more details on the model generation process, the reader is referred to Pro and Barthelat (2019).

The interfaces were modeled with a phenomenological trapezoidal cohesive law (Fig 2a) that is fully characterized by a stiffness k (initial slope), strength σ_0 (peak stress), and fracture energy Γ_i (area under the cohesive curve). The interface area is shown in Fig. 2a and is defined as a 2D rectangular area $A_i=h_e l_i$, where h_e is the mesh size (Fig. 1b) and li is the length of the edge that intersects that interface in the corresponding Voronoi contour. The underlying assumptions and idealizations of the interfaces are identical to our previous work (Pro and Barthelat, 2019) with one addition: in the dynamic formulation

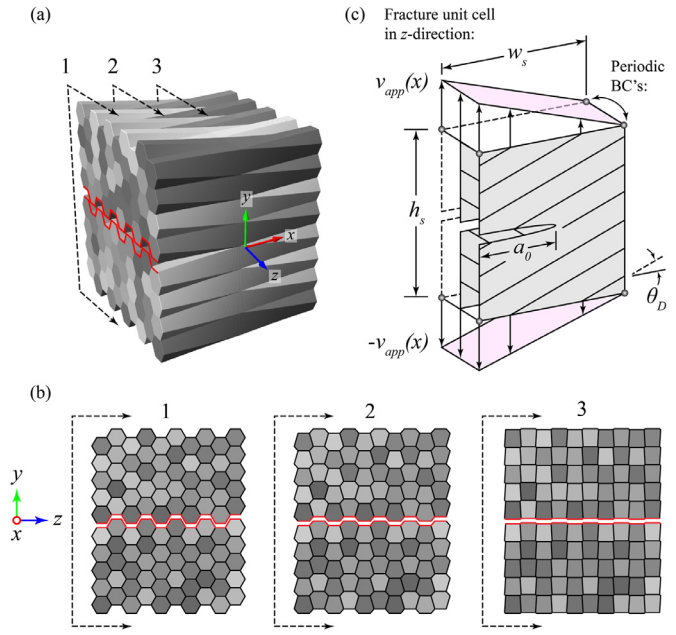

Fig. 3. (a) Full 3D generated enamel rod geometry with decussation and (b) cross section slices at various locations in the yz-plane in the direction of crack growth. (c) Shows the modeled specimen with dimensions and boundary conditions.

the interfaces are assumed to be massless which is reasonable given their low volume fraction (Maas and Dumont, 1999). The enamel rods were modeled in the same manner as our previous study (Pro and Barthelat, 2019) using 3D Bernoulli-Euler beam elements except rod inertia was included and brittle rod fracture were accounted for in this study. The rod elements were assigned a density σ_r and assumed to be initially linear elastic (modulus E_r) up to an ultimate strength of σ_{ru}, at which point the load instantly drops to zero (brittle fracture) and that rod element is erased from the simulation permanently. This model of rod fracture is highly idealized and neglects the details of intermediate crack growth within the enamel rods, and assumes that rod fracture is always unstable: if any flaw within the rod is activated due to local stress intensities, then it is assumed that the flaw grows catastrophically and instantaneously fractures the entire cross section of the rod. This assumption is valid in the limit that the limiting crack velocity within rods (dictated by the Raleigh wave speed (Xu and Needleman, 1994)) is much higher than that of the interfaces, which is related to the elastic mismatch between the two materials (up to 100–1000 in natural hard/soft composites (Barthelat, 2015; Pro et al., 2015b)).

To capture fracture properties and crack propagation, we generated a large volume of the microarchitecture in Fig. 1 into a virtual fracture specimen (height hs, width ws) with an initial edge pre-crack of length $a_0=w_s/2$ (Fig. 3). The dimension in the z-direction (thickness) was assumed to be infinite and therefore periodic boundary conditions were implemented in the z-direction with constraint equations. Velocity boundary conditions were applied along the lower and upper faces and followed a linearly graded spatial distribution from left to right (peak applied velocity v_{app}, Fig. 3), in order to promote stable crack growth (Pro and Barthelat, 2019; Pro et al., 2015a; Abid et al., 2019; Pro et al., 2015b; Tada et al., 1973).

To maintain quasi-static loading conditions, vapp was kept small relative to the characteristic wave speed c_d ($v_{app}/c_d \approx 0.001$) which was approximated from the uniaxial wave speed:

$$c_d = \sqrt{\frac{E_{transverse}}{\rho_r}} \tag{1}$$

Where $E_{transverse}$ is the modulus in the pulling direction and was obtained from our previous study on enamel moduli (Pro and Barthelat, 2019). Proportional damping was implemented to eliminate unwanted high frequency dynamic effects and to allow larger load rates to be applied while still maintaining quasi-static loading conditions (Pro et al., 2018, Cook et al., 1974, Sehr et al., 2019). The dimensionless damping ratio is denoted as ξ and is given from the damping coefficients as a function of structural frequency ω as (Cook et al., 1974):

$$\zeta = \frac{1}{2}\left(\frac{\beta}{\omega} + \alpha\omega\right) \tag{2}$$

Where α and β are the mass and stiffness damping terms, respectively. We assumed that the damping ratio was a minimum at the lowest natural frequency ω_{min} (where ω_{min} was approximated from the largest specimen dimension), which

gives the structural damping coefficients from Cook et al. (1974) as:

$$\alpha = \sqrt{\frac{\pi^2 \zeta^2 E_{transverse}}{h_s \rho_r}},\ \beta = \sqrt{\frac{\zeta \rho_r h_s}{\pi^2 E_{transverse}}} \tag{3}$$

A conservative damping ratio of ζ=0.2 was used in all calculations. In general, the dynamic response of a structure under loading depends on the specific level of damping which is governed by physical material constants (Paz, 1985). However in the quasi-static limit of slow loading, the choice of damping coefficients becomes arbitrary (Prior, 1994) as the velocity and acceleration become negligible. We verified for most calculation results that this limit was achieved by running a case with a 1/2x slower load rate and comparing the crack resistance curves. A few cases were also validated against our previous quasi-static results (Pro and Barthelat, 2019) and gave numerically indistinguishable results. We note that the dimensionless damping ratio ζ and loading rate v_0/c_d and were both based on approximation expressions and some trial and error was required to obtain quasistatic results. At all loading increments, the position of the crack tip was tracked and the 3D J-integral was calculated at the outermost boundary of the specimen as in Pro and Barthelat (2019), Abid et al. (2019). The fracture length along the interfaces was set to be large relative to the mesh but small relative to the specimen size hs (Parmigiani and Thouless, 2006, Parmigiani and Thouless, 2007) such that it did not affect the calculation results; as in Pro and Barthelat (2019), this was checked with trial and error by running large and small specimens and coarse ($h_e/d \approx .3$) and fine meshes ($h_e/d \approx 0.15$).

The full governing dynamic equations of motion (with inertial terms) were solved directly with explicit dynamic time integration. We used this approach to eliminate convergence issues associated with incremental, gradient based numerical schemes (Press et al., 2007) when modeling instabilities. Indeed, when implementing the brittle rod constitutive law in our previous implicit-based models Pro and Barthelat (2019), we experienced convergence issues caused by local instabilities in microfracture events that led to exceedingly large simulation times. These instabilities are in fact manifestations of real effects: when a microflaw is activated within a rod, its stability is governed by a local criteria ($dG_{flaw}/da < dR_{flaw}/da$) rather than a global stability criteria ($dG/da < dR/da$) (Anderson, 2017). For very stiff and brittle rods, this often implies that local rod fracture is unstable until the initiated microflaw reaches the edges of the entire rod, which occurs over very short time scales compared to other structural time scales. These instabilities are inevitable and cannot be eliminated by altering the global loading configuration or reducing the global loading rate, but do not influence the results in the limit of slow loading; hence the use of an explicit DEM approach is justified.

The explicit time integration DEM scheme followed an identical assembly procedure as standard finite element analysis. The global stiffness, mass, and damping matrices for the rods only (denoted as [K]r, [M]r, and [C]r, respectively) were first assembled as follows:

$$[K]_r = \sum_{i=1}^{n_e} [K]_{r,i} \tag{4}$$

$$[M]_r = \sum_{i=1}^{n_e} [M]_{r,i} \tag{5}$$

$$[C]_r = \sum_{i=1}^{n_e} [C]_{r,i} \tag{6}$$

Where $[K]_{r,i}$, $[M]_{r,i}$, $[C]_{r,i}$ are the local elemental stiffness, mass, and damping matrices for rod element i, respectively and ne is the number of rod elements. The local elemental proportional damping matrix $[C]_{r,i}$ is given as:

$$[C]_{r,i} = \alpha_{r,i}[M]_{r,i} + \beta_{r,i}[K]_{r,i} \tag{7}$$

Where $\alpha_{r,i}$ and $\beta_{r,i}$ are the mass and stiffness damping coefficients of rod i, respectively. The interfaces were assumed to be massless and therefore only contributed a stiffness term. For computational efficiency the interface local stiffness matrices were never formed. Rather, the interface forces were computed directly from the nonlinear cohesive law in Fig. 2a and applied as a set of equal and opposite internal forces (Cook et al., 1974) to avoid constant updating of the global stiffness matrix during interface rupture. The local internal interfaces forces were assembled into the global internal interface force vector as:

$$\{f\}_{iface} = \sum_{i=1}^{n_i} \{f\}_{iface,i} \tag{8}$$

Where $\{f\}_{iface,i}$ represents the internal force vector for a single interface i, $\{f\}_{iface}$ is the global assembled interface force vector, and ni is the number of interfaces. The full system of governing dynamic ODE's is then given in discretized matrix-vector form as:

$$[K]_r\{q\} + [C]_r\{\dot{q}\} + [M]_r\{\ddot{q}\} + \{f\}_{iface} = \{f\} \tag{9}$$

Where $q, \dot{q}$, and $\ddot{q}$ are the vectors of nodal displacements, velocities, and accelerations, respectively, and {f} is the vector applied external forces. Making the following substitution:

$$\{R\} = \{f\} - \{f\}_{iface} - [K]_r\{q\} - [C]_r\{\dot{q}\} \tag{10}$$

and rearranging Eq. (9) gives the following:

$$[M]_r\{\ddot{q}\} = \{R\} \tag{11}$$

Where {R} is the nodal reaction force vector. Displacement boundary conditions and nodal ties were formulated into linear constraint equations that were applied by augmenting Eq. (11) with Lagrange multipliers (Pro and Barthelat, 2019). The full displacement and velocity vectors were then updated numerically using the Newmark-β method with β=0, where the subscripts $n+1$ and n denote the solutions at the new and previous time step respectively:

$$\{q\}_{n+1} = \{q\}_n + \Delta t\{\dot{q}\}_n + \frac{1}{2}\Delta t^2\{\ddot{q}\}_n \tag{12}$$

$$\{\dot{q}\}_{n+1} = \{\dot{q}\}_n + \frac{1}{2}\Delta t\left(\{\ddot{q}\}_n + \{\ddot{q}\}_{n+1}\right) \tag{13}$$

To solve explicitly for $\{\ddot{q}\}_{n+1}$, Eq. (9) was substituted into Eq. (13)

$$\{\ddot{q}\}_{n+1} = [H]^{-1}\left(\{f\} - \{f\}_{\text{int}} - [K]_r\{q\}_{n+1} - [C]_r\{q_n + \frac{1}{2}(\Delta t)\ddot{q}_n\}\right) \tag{14}$$

Where the following substitution was made:

$$[H] = [M]_r + \frac{1}{2}\Delta t[C]_r \tag{15}$$

For improved efficiency and accuracy we computed only the lower-upper (LU) factorization of [H] rather than its inverse, and re-used this factorization at every time step to perform a direct triangular solve of Eq. (14) (Press et al., 2007). The maximum rod stress $\sigma_{r,\,max}$ was computed in all rods and if any rod element i* exceeded its ultimate strength σ_{ru} (Fig. 2), it was subtracted from the simulation:

$$[K]_r = [K]_r - [K]_{r,i*} \tag{16}$$

$$[M]_r = [M]_r - [M]_{r,i*} \tag{17}$$

$$[C]_r = [C]_r - [C]_{r,i*} \tag{18}$$

The [H] matrix was then updated, re-factorized, and stored, which only occurred approximately every thousand (out of millions) time steps and did not introduce substantial computational expense. The procedure described in Eqs. (12)–(18) was iterated over a full time-stepping loop with regular file-writing intervals. The algorithm was implemented in C++ and used the UMFPACK library for sparse LU factorization (Davis, 1993). Linux shell scripts (.sh) were used for automating simulations and the calculations were performed on the Graham and Cedar supercomputers using Compute Canada resources. A typical simulation required about 400 rods (rod length ~ 200d) and 1200 interfaces, discretized with about 120,000 total beam elements and 380,000 total interface elements (respectively) in order to achieve specimen and mesh size independent results with respect to the fracture length (Pro et al., 2018; Parmigiani and Thouless, 2006; Parmigiani and Thouless, 2007). This discretization implied about 200,000 total nodes with 6 DOF's per node (three displacements and three rotations) resulting in stiffness, mass, and damping matrix sizes of about 1.2 by 1.2 million. For numerical stability the time step size Δt was set at about one-tenth of the lowest natural period of a single rod beam element (Cook et al., 1974), and combined with the requirement for slow loading (Eq. (1)) implied about 3 million total iterations of the time-stepping algorithm. These four requirements (specimen size, mesh size, time step size, and slow loading) scaled the total run-time which was about 3.5 days for an average simulation. Around 200 fracture simulations were run in preparing this work, run in batches of about 25 simultaneous simulations at a time on the clusters for about one month of straight computation wall time. The graphical output was postprocessed using Paraview (Ahrens et al., 2005). Using the explicit DEM algorithm, we carried out two main types of virtual fracture tests: uniform distribution of rod strengths (Sections 3–5) and statistical (random) distribution in rod strengths (Section 6).

3. Effect of the decussation angle θ_D

It is known from experiments (Bajaj and Arola, 2009a; Yahyazadehfar et al., 2013; Bajaj and Arola, 2009b, Bajaj et al., 2010) and models (Pro and Barthelat, 2019) that rod decussation provides a major obstacle for crack propagation. At a basic level, adjacent rods interact through friction, viscous fluid-to-solid interaction, and mineral bridges that generate inelastic deformation and toughness along a crack front between rods. A crack entering the decussating region can kink and/or branch along non-planar interfaces introduced through the complex 'woven' architecture (Bajaj and Arola, 2009;

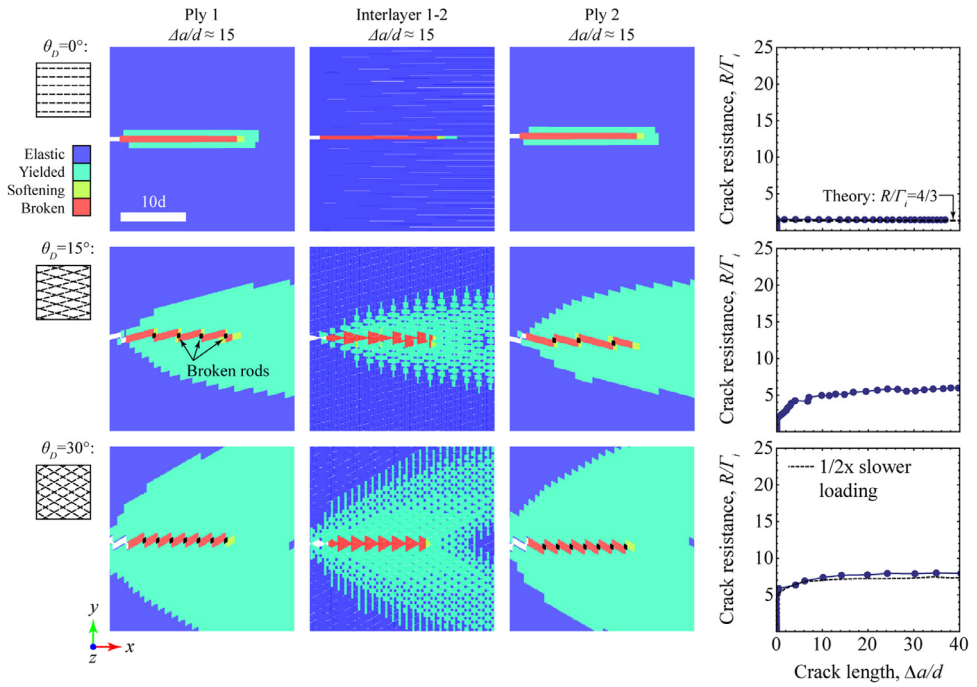

Fig. 4. Effect of the decussation angle θ_D for fixed strength contrast ($\sigma_{ru}/\sigma_0 = 21.4$) and fixed stiffness contrast (E_r/kd=10). Snapshots of the emergent crack patterns and through-thickness process zone contours are shown in the first 3 columns alongside their corresponding crack resistance curves in the last column, with broken rod elements highlighted in black. The last interlayer is not shown as it was indistinguishable from interlayer 1–2 in all cases. For θ_D =30° we also show a case with 50% slower loading to verify the results are quasi-static.

Yahyazadehfar et al., 2013; Bajaj and Arola, 2009b, Bajaj et al., 2010), which can delay crack propagation and spread inelastic energy dissipation over larger length scales (process zone) while simultaneously increasing the elastic stresses on the hard phase (Abid et al., 2019; Pro et al., 2015; Barthelat and Rabiei, 2011). This crack propagation mechanism creates a complex competition of failure modes that is a function of the decussation angle (θ_D) and the relative contrasts between the rod and interface in terms of strength (ratio $\frac{\sigma_{ru}}{\sigma_0}$) and stiffness (ratio E_r/kd). In this first set of simulations (Fig. 4) we explore the effect of decussation for fixed strength contrast ($\frac{\sigma_{ru}}{\sigma_0} = 21.4$) and fixed stiffness contrast (E_r/kd=10).

For the case with no decussation ($\theta_D = 0^0$, first row in Fig. 4), the crack propagated between and parallel to the rods with relatively little inelastic deformation. The crack resistance curve did not show any evidence of toughening: Initiation toughness and steady state crack resistance (denoted as R_{init} and R_{ss}, respectively) were identical and equal to the theoretical delamination toughness ($\frac{R theory}{\Gamma_i} = 4/3$). The theoretical delamination toughness for $\theta_D = 0^0$ is higher than unity because the corrugated crack faces (Fig. 3a) introduce 4/3x more crack surface area per unit crack advance in the x-direction than that of a flat crack (Anderson, 2017).

For $\theta_D > 0^0$ we observed that for $\Delta a < \frac{d}{\sin(\theta_D)}$ the pre-crack initially formed two kinks along interfaces between rods oriented at $\pm\,\theta_D$ in the first and second plies respectively, without fracturing any rods. As the projected position of the kinked crack tips on the x-axis reached the nearest crisscrossing point (defined as the points where the rod centerlines at $+\theta_D$ cross those at $-\theta_D$, spaced at integer multiples of $\frac{d}{\sin(\theta_D)}$ in the horizontal direction) along the specimen mid-plane, the interfaces directly ahead of both kinks softened which redistributed and concentrated the maximum model stress directly to the rod elements at that crisscrossing point. Eventually these rods fractured and both kink tips were simultaneously jolted downward/upward by one rod diameter. This process was repeated as the load was applied which formed an overall crack with a periodic 'sawtooth' pattern of broken interfaces and rods. In the interlayer, the crack path consisted of only broken interfaces and formed a merged-sawtooth wave with the same frequency as the interface/rod cracks in the plies. The overall frequency of the sawtooth crack matched the characteristic decussation frequency f_D given by the geometry of the microstructure: $f_D = \frac{\sin(\theta_D)}{d}$.

In terms of crack resistance, nonzero decussation increased the initiation toughness because the rod crisscrossing points served as added obstacles for crack initiation (Fig. 4) that forced the inelastic region to develop along forked/branched interfaces through pinning rather than along a perfectly straight Mode I plane. Similarly, during crack propagation, decussation initially delays straight crack propagation and forces a 3D forked crack to develop along the same forked interfaces. The forked crack configuration requires more energy for sustained growth than a straight crack and therefore spreads inelasticity over larger volumes, initially leading to toughening and rising R-curves (Fig. 4). When rod fracture initiates a straight crack (on average) emerges which is a lower energy state (lower toughness) than the forked configuration; growth of the

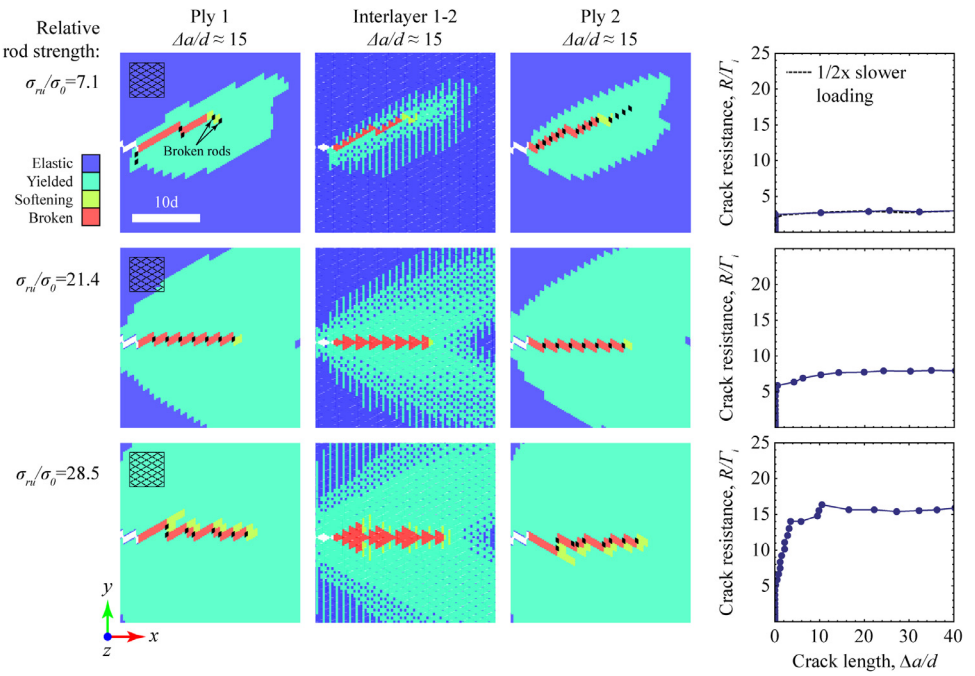

Fig. 5. Effect of normalized rod strength σ_{ru}/σ_0 on crack propagation, development of a nonlinear inelastic region (process zone) ahead of the crack tip, and crack resistance. For all cases shown, $\theta_D = 30^0$ and $E_r/kd=10$. For the lowest strength ($\sigma_{ru}/\sigma_0 = 7.1$) modeled, a case with a 50% slower loading is also shown for verification.

inelastic region is inhibited while the system reaches a steady state crack resistance $\frac{R}{\Gamma_i} \approx 7$ for ($\theta_D = 15^0$) and $\frac{R}{\Gamma_i} \approx 7$ for $\theta_D = 30^0$ (at $\frac{\Delta a}{d} \approx 15$).

4. Effects of relative rod strength σ_{ru}/σ_0

Crack propagation and toughening are governed by two competing failure mechanisms: the fracture of individual rods and the yielding/failure of the interfaces. The details of this competition can be captured in our models by tuning the relative strength of rods and interfaces. Fig. 5 shows the through-thickness process zone contours (columns 1–3 for $\frac{\Delta a}{d} = 15$) and corresponding R-curves (column 4) for three contrasts of strength σ_{ru}/σ_0 at a fixed decussation $+\theta_D$ and fixed stiffness contrast ($E_r/kd=10$).

For the lowest relative rod strength ($\sigma_{ru}/\sigma_0 = 7.1$) the crack kinks at $+\theta_D$ through the thickness of the specimen with a limited process zone size. The 3D crack grows parallel to the rods in the first ply, with only a few broken rods in that layer. In the second ply the crack followed the same general direction, forcing crack propagation across the rods. As a result, the crack in that ply alternated between fracturing rods and fracturing interfaces. In this case the symmetry is broken when the crack propagates even though the loading and microstructure are symmetric (Mode I) due to unstable equilibrium, which is governed by both the strength and stiffness contrast. This is analogous to a simple system of three nonlinear springs in series: as the spring strength contrast is reduced (analogous to low $\frac{\sigma_{ru}}{\sigma_0}$), the symmetric deformation state is introduced (all three springs breaking simultaneously) but as an unstable equilibrium solution, therefore for lower $\frac{\sigma_{ru}}{\sigma_0}$ the non-symmetric fracture modes are much more likely even when the system is initially symmetric.

For moderate strength contrasts ($\sigma_{ru}/\sigma_0 = 21.4$) the same case is shown as in Fig. 4 for $\theta_D = 30^0$ but is used here for cross-comparison against different strength contrasts instead of decussation and reveals new insight: as the strength contrast is increased 'controlled' crack propagation is achieved as the symmetric (Mode I) deformation state becomes a stable equilibrium solution, analogous to the three springs in series system but where the outer springs are made stronger. The main crack remained pinned longer as the rod elements at the crisscrossing point nearest to the pre-crack could now sustain higher loads, which led to the spreading of the inelastic region over larger length scales and higher crack resistance (up to $\frac{R}{\Gamma_i}$ for $\theta_D = 30^0$ at $\frac{\Delta a}{d} > 15$). For the highest strength contrast modeled ($\frac{\sigma_{ru}}{\sigma_0} = 28.5$), the initial pair of kinks grew past the first crisscrossing point nearest to the pre-crack ($\frac{\Delta a}{d} \approx 4$ for $\theta_D = 30^0$) at which point the crack resistance temporarily reached a constant value while the interface kinks continued to grow. The stress was then redistributed to the next nearest crisscrossing point directly ahead of the main crack (along the specimen mid-plane) which re-initiated the growth of the inelastic region and was accompanied by a rise in crack resistance (starting at $\frac{\Delta a}{d} \approx 4$ in Fig. 5 row 3). Eventually the stress

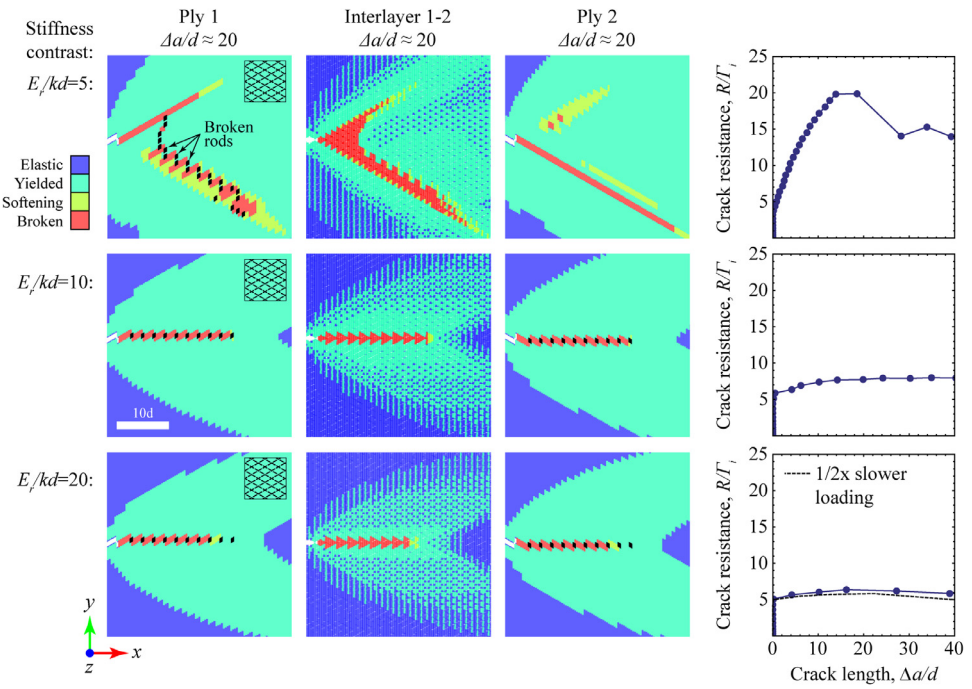

Fig. 6. Effect of stiffness contrast for fixed decussation and rod strength ($\theta_D = 30^0$ and $\sigma_{ru}/\sigma_0 = 21.4$). The crack path and inelastic region distribution are shown in columns 1–3 alongside the corresponding R-curves in column 4.

'pile-up' caused successive fracture of rods at the crisscrossing points directly ahead of the pre-crack and an overall straight crack eventually emerged.

The crack path for $\theta_D = 30^0$ is more complex and contains higher frequencies as the occurrences of rod and interface fracture are asynchronous. Combined with the effect of decussation, higher strength contrast delays the development of a full through thickness crack and forces the initial interface fork to grow larger while spreading inelasticity over larger length scales. When rods begin to fracture the inelastic region cannot sustain continued growth and the system reaches a steady state crack resistance (around $\frac{\Delta a}{d} \approx 15$ for most cases), which increased in all cases with increasing strength contrast. The initiation toughness (R_{init}) also increased with strength contrast but for $\frac{\sigma_{ru}}{\sigma_0}$, the interfaces always fractured before any rods therefore $\frac{\sigma_{ru}}{\sigma_0}$ had no effect on R_{init}.

Interestingly the simulations also showed that strength contrast introduced preferential fracture planes influenced by the microstructure, which was particularly evident for low strength contrasts ($\frac{\sigma_{ru}}{\sigma_0} <= 7.1$). Indeed experimental evidence has suggested that preferential wear is the key to the 'self-sharpening' mechanism in mouse incisors (Cox, 2010; Boyde, 1989): as the enamel wears, entire 'sheets' of rods cleave from the outermost surface in a controlled manner such that the tip of the tooth maintains its sharpness. The DEM simulations suggest that both strength contrast and decussation play a role in the preferential wear of enamel; this mechanism could be modeled and confirmed with similar but more detailed DEM fracture simulations that account for the tooth geometry as well as nucleation and fracture of cleavage planes.

5. Effects of relative rod stiffness E_r/Kd

The mechanism of crack propagation is also function of how the applied stresses are channeled in the rods and in the interfaces, and this distribution of stresses is governed by the relative stiffness of the rods and interfaces (stiffer rods will carry more of the applied stress). We explored the effect of the relative stiffness of the rods by tuning the parameter E_r/kd between 5 and 20, which is a reasonable range considering the composition of enamel (Pro and Barthelat, 2019; Spears, 1997). Fig. 6 shows the effects of E_r/kd on crack propagation and toughness for a fixed decussation angle ($\theta_D = 30^0$) and a fixed relative rod strength ($\sigma_{ru}/\sigma_0 = 21.4$). For the lowest stiffness contrast modeled (E_r/kd = 5), the initial 3D crack consisted of only ruptured interfaces that formed a pair of kinks at $\_\theta_D$ in the first and second ply, respectively. In this case the kinks grew well past the first crisscrossing point of rods directly ahead of the crack tip while the crack resistance and inelastic region simultaneously increased for $\frac{\Delta a}{d} \approx 15$ (Fig. 6).

At about $\frac{\Delta a}{d} \approx 15$, the first rod fractured ahead of the upper kink causing it to suddenly deflect downward and merge with the lower kink to form a single through thickness crack at $-\theta_D$. The final crack consisted of both broken interfaces and rods in the first ply (against the grain), and only broken interfaces in the second ply (delamination). This progression of crack propagation is qualitatively similar to those observed in fracture experiments of engraved laminated glass crossply compos-

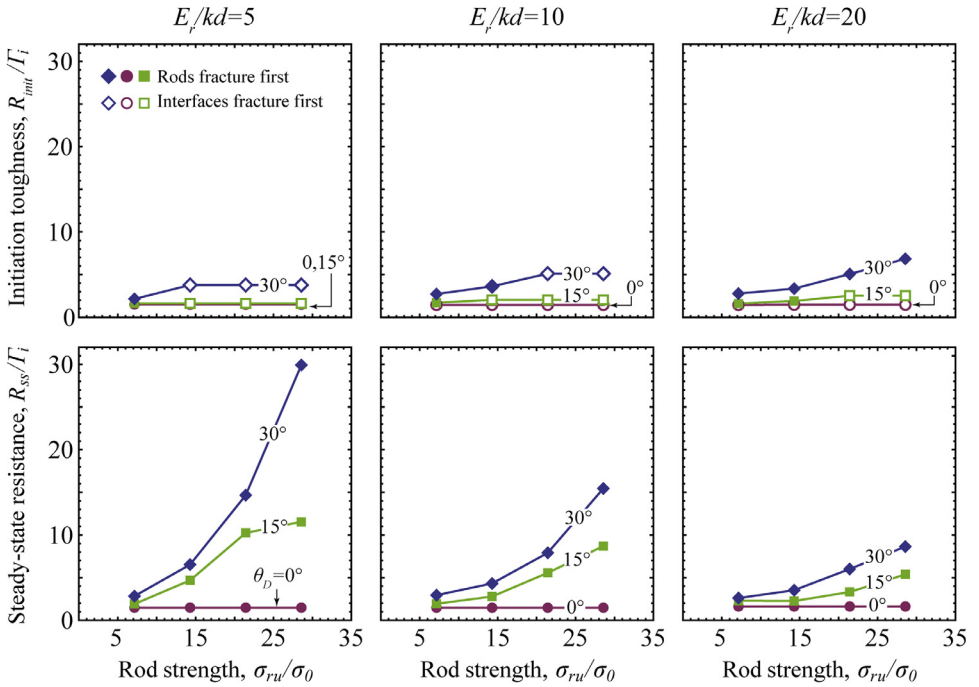

Fig. 7. Initiation toughness R_{init}/Γ_i and steady state crack resistance R_{ss}/Γ_i as a function of decussation angle θ_D, rod strength σ_{ru}/σ_0, and stiffness contrast E_r/kd, where the cohesive law strength σ_0, stiffness k, and fracture energy Γ_i (Fig. 2) were again used as normalizations. The initiation toughness R_{init}/Γ_i is computed at the first increment in crack advance where $\Delta a/d > 0$. For comparative purposes the crack resistance curves are represented by a single data point at $\Delta a/d \approx 30$ which is defined as R_{ss}/Γ_i.

ites we recently reported (Yin et al., 2018): the crack initially forms a partially-kinked partially-branched configuration; as the branch grows the equilibrium state becomes more unstable but at elevated energy (higher toughness). Eventually small defects force the branch to 'choose' a direction and the solution is forced into a lower energy state (local minima) with lower toughness.

For higher stiffness contrasts (E_r/kd=10, 20), the rods carry higher fractions of the applied stresses. As a result the rods fracture before the main crack reaches the nearest crisscrossing point, and before the unstable equilibrium branch can develop. The resulting crack grows in a controlled and periodic 'sawtooth' pattern but with lower crack resistance and a smaller inelastic region ($\frac{R}{\Gamma_i} \approx 8$ for $E_r/kd = 10$ and $\frac{R}{\Gamma_i} \approx 6$ for $E_r/kd = 20$, both at $\frac{\Delta R_m}{\Gamma_i} \approx .4$). We note that our previous models with infinite rod strength ($\frac{\sigma_{ru}}{\sigma_0}$) showed that stiffness contrast alone increased the crack resistance (Pro and Barthelat, 2019) but also elevated the stress state within the rods. Our new models here show that rod fracture always limits the crack resistance (e.g., Fig. 5); therefore stiffness contrast and rod fracture present competing toughening and embrittlement mechanisms, respectively. When modeled simultaneously, the embrittlement contribution due to rod fracture exceeds the toughening contribution from stiffness contrast leading to an overall net decrease in crack resistance reflected in Fig. 6. Stiffness contrast expedites rod fracture which releases stresses that would otherwise drive further growth of the inelastic region, ultimately limiting the crack resistance.

Fig. 7 provides a summary of the effect of decussation angle, relative rod strength and relative rod stiffness on initiation toughness (R_{init}) and steady state toughness (R_{ss}). The initiation toughness R_{init} initially increases with contrast in strength (rods fracture first) but reached a constant plateau (interfaces fracture first) for high enough rod strength (e.g., $\frac{\sigma_{ru}}{\sigma_0} = \geq 21.4$ for E_r/kd=10 and $\theta_D = 30^0$). In the latter limit, the rod strength is high enough that initiation of an interface crack occurs before the rod elastic stresses exceed the rod strength; therefore increasing the rod strength further has no effect on the calculation results. For higher stiffness contrasts, higher strengths were required to reach this limit, and in some cases it was never reached (e.g. E_r/kd=20 and $\theta_D = 15^0, 30^0$). When the rods fractured first, there was little difference between two cases with different stiffness contrast but the same strength and decussation angle. In all cases the steady state crack resistance R_{ss} increased with the relative rod strength $\Delta\sigma_{ru}/\bar{\sigma}_{ru}$ and decussation angle θ_D but decreased with stiffness contrast E_r/kd. This result illustrates a conflicting design tradeoff for bioinspired composites: for maximum crack resistance the rods should be both compliant and strong, two mechanical properties which are typically mutually exclusive (Ashby and Cebon, 1993). Moreover, lowering the stiffness contrast lowers the overall modulus (Pro and Barthelat, 2019) which is often undesirable.

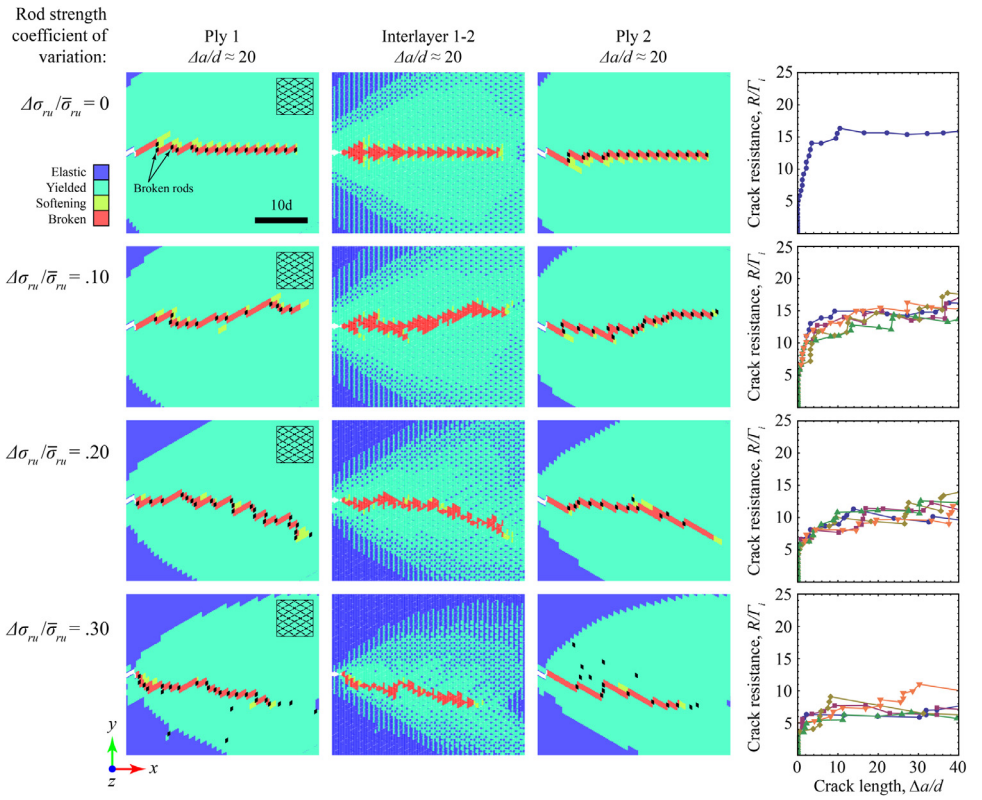

Fig. 8. Effect of rod strength coefficient of variation $\Delta\sigma_{ru}/\overline{\sigma}_{ru}$ on crack path, inelastic zone, and crack resistance for fixed population mean in rod strength ($\overline{\sigma}_{ru}/\sigma_0 = 28.5$), fixed decussation ($\theta_D = 30°$), and fixed stiffness contrast (E_r/kd=10). The snapshots show typical simulation results from a single microstructure realization at various coefficients of variation, with all five realizations shown in the corresponding R-curves.

6. Effects of statistical rod strength distribution

We now consider cases with statistical spatial distributions of strength within the rods to model the effect of flaws, defects, and other inhomogeneities within the mineral rods. The simulation procedure and model setup are identical to that in the previous section except the rod element strengths are generated from a random normal distribution, with the normalized population mean in rod strength denoted as $\frac{\bar{\sigma}_{ru}}{\sigma_0}$ and coefficient of variation (CV) as $\frac{\Delta\sigma_0}{\bar{\sigma}_{ru}}$, where $\Delta\sigma_{ru}$ is the population standard deviation. For each different coefficient of variation we generated and simulated five realizations from the same population mean and standard deviation as in (Abid et al., 2019). For proper comparisons we kept the specimen size w_s and h_s constant as it is well known that brittle materials with statistically distributed flaws exhibit size-dependent failure properties (Bažant, 1984; Bažant, 2004). Additionally, in brittle materials the volumetric density of flaws affects the average failure properties (Danzer, 1992), which was modeled with the rod element mesh size h_e. Finer meshes (smaller h_e) represent a material with higher flaw density and therefore the statistical probability of sampling a larger critical flaw is higher (Zhou and Molinari, 2004). In many brittle systems it is not uncommon for flaw sizes to be on the order of nanometers which would require prohibitively fine meshes to realistically model even with the most powerful supercomputers. Here we implement much coarser meshes which keeps the simulation cost manageable but overestimates the true fracture properties (Zhou and Molinari, 2004). For consistent comparison between different models, identical meshes were used across all models in this section. Moreover, in all calculations the element size he was uniform over the entire volume of the specimen. We did not attempt mesh convergence for these statistics based calculations (over 4 weeks run-time) and it was assumed for convenience and simplicity that the mesh size established for the section with no statistics ($h_e/d = 0.3$) was sufficient as it yielded numerically convergent R-curves. These simplifications eliminated the need to use element-size dependent statistical calculations (as in conventional Weibull-based finite element simulations (Zhou and Molinari, 2004)): the mesh size h_e was in fact constant for all elements within all models shown in this section.

Fig. 8 shows the effect of the coefficient of variation in rod strength on crack propagation, inelastic region, and crack resistance for four different coefficients of variation ranging from $0 \leq \Delta\sigma_{ru}/\bar{\sigma}_{ru} \leq 0.3$. For each CV, R-curves from all five microstructure realizations are shown alongside typical simulation contours from a single realization. For $\Delta\sigma_{ru}/\bar{\sigma}_{ru} > 0$, the crack path differed substantially from one realization to the next but on average the evolution and size of the inelastic region was relatively unchanged. For low to moderate coefficients of variation ($.1 \leq \Delta\sigma_{ru}/\bar{\sigma}_{ru} \leq .2$), rod fracture was observed

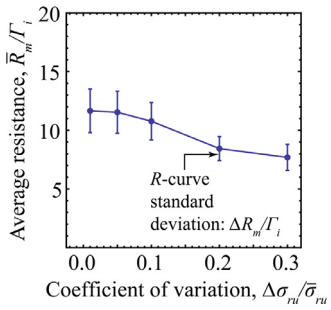

Fig. 9. Effect of coefficient of variation in rod strength $\Delta\sigma_{ru}/\bar{\sigma}_{ru}$ on the average merged crack resistance $\bar{R}_m/\Gamma_i$, where $\bar{R}_m/\Gamma_i$ included data from all realizations over the subset of crack advance $0 < \Delta a/d < 30$. The error bars show the standard deviation in the merged crack resistance data, $\Delta R_m/\Gamma_i$.

only very locally in the highest stressed region ahead of the crack tip. In this case the statistical distribution in rod strength was narrow enough that the rod elements in the lower stressed elastic region (e.g., far from the crack tip) had a lower (but nonzero) probability fracturing before those in the region of maximum stress; the probability was low enough that it was not observed over the course of the simulation and the elastic stress distribution governed the failure sequence of rods rather than inhomogeneities in strength. For high coefficients of variation ($\Delta\sigma_{ru}/\bar{\sigma}_{ru} \geq .2$), weak sections of rods began to fracture farther from the main crack before the main crack advanced, which was particularly evident for $0.1 < \Delta\sigma_{ru}/\bar{\sigma}_{ru} < 0.5$. For these cases there is a higher probability that the stress failure criterion for rods far from the crack tip is met before the energy criterion for advance of the main crack is met. This long-range formation of daughter cracks is simply due to probability: for wider distributions (e.g., with greater $\Delta\sigma_{ru}/\bar{\sigma}_{ru}$) the area under the left tail of the probability density function is increased. As daughter cracks nucleate, weak planes ahead of the main crack are formed which the main crack tends to follow, coalescing with the daughter cracks as it advances which inhibits the spread of the inelastic region and overall decreases the toughness. This conclusion is qualitatively similar to those reached in our previous DEM models of nacre-like materials (Abid et al., 2019) that considered only interface fracture with statistical distributions in tablet size.

Interestingly however, previous analyses of synthetic fiber-matrix composites have illustrated that variability in fiber strength can in fact increase toughness, depending on the fiber size and relative fiber to matrix strength ratio (Thouless and Evans, 1988). This differs from the conclusions reached here but we note several apparent differences. First, the analysis of Thouless and Evans (1988) assumed a vertical unidirectional fiber-matrix composite, whereas the structures here are assumed to be decussating crossplies. Additionally, modern composites contain much higher volume fractions of the soft phase (e.g., matrix or interface) than natural biocomposites, which is typically on the order of 35–50% (Gibson, 2016) (compared to 1–5% in most hard biological composites (Yahyazadehfar and Arola, 2015)). These differences lead to substantially different toughening mechanisms in enamel (bridging, deflection/branching (Bajaj and Arola, 2009a)) compared to modern fibrous composites (fiber-pullout, fiber/matrix frictional sliding, crack front/wake debonding (Evans and Zok, 1994)), which in turn alters the impact of statistics on the respective composites. In particular the higher matrix volume fraction in engineered composites reduces stress transfer to the fibers themselves (fibers carry less load) (Gibson, 2016), which increases the overall probability that a weakest-link flaw can stabilize itself post-initiation (Anderson, 2017) and provides a basic mechanism for delaying localization in the fibers. We also note that enamel interfaces are governed mostly fluid to solid interactions and friction whereas in modern composites the fibers are embedded in a continuous matrix; the latter can support more complex stress states and therefore also contribute to stabilization of flaws. Indeed experimental evidence has indicated that microcracks can spread over larger length scales (~1 mm) in engineered composites (Evans and Zok, 1994; Evans, 1991), whereas enamel microcracking is relatively localized (Lawn et al., 2009). In general the nature of microcracking is different in the two systems which makes statistics advantageous for engineered composites but detrimental in natural systems.

Fig. 9 summarizes the effect of the coefficient of variation on the average merged crack resistance $\frac{\bar{R}_m}{\Gamma_i}$, taken from data over all statistical realizations over the interval $0 < \frac{\Delta a}{d} < 30$ for each realization. For low nonzero coefficients of variation ($0 < \Delta\sigma_{ru}/\bar{\sigma}_{ru} < 0.5$) the average merged crack resistance is relatively insensitive to $\Delta\sigma_{ru}/\bar{\sigma}_{ru} \geq 0$ ($\frac{\bar{R}_m}{\Gamma_i} \approx 11.9$) but decreases on the order of 50% for higher coefficients of variation; this is on the same order of magnitude of the reductions in toughness reported by Abid et al. (2019) and Pro et al. (2015a) in similar DEM simulations of nacre-like composites. To illustrate the predictability in crack resistance, the standard deviation in the merged R-curve data (denoted as $\frac{\Delta R_m}{\Gamma_i}$) is also shown on Fig. 9 as error bars. Interestingly, the deterministic case showed the largest $\frac{\Delta R_m}{\Gamma_i}$ and $\frac{\Delta R_m}{\Gamma_i}$ decreased by about 50% for higher coefficients of variation ($\frac{\Delta R_m}{\Gamma_i}$ for $\Delta\sigma_{ru}/\bar{\sigma}_{ru} = 0.3$ to $\frac{\Delta R_m}{\Gamma_i} \approx .2$ at $\Delta\sigma_{ru}/\bar{\sigma}_{ru} \geq .2$). This data illustrates an important result: the transient nature of the R-curve for $\Delta\sigma_{ru}/\bar{\sigma}_{ru} \geq 0$ introduces a large enough $\frac{\Delta R_m}{\Gamma_i}$ that any nonzero coefficient of variation in fact reduces $\frac{\Delta R_m}{\Gamma_i}$. This is in part because the maximum crack resistance (and therefore the span between the maximum and minimum crack resistance, related to $\frac{\Delta R_m}{\Gamma_i}$) is also reduced. This result shows a fundamental tradeoff

between properties: on average the material is tougher for lower coefficients of variation but less predictable (in terms of a higher $\frac{\Delta R_m}{\Gamma_i}$) as the crack advances, and vice versa for higher coefficients of variation .

7. Summary and conclusions

The models here illustrate the competing effect of rod and interface fracture on the tradeoffs in crack resistance in decussating enamel structures, and show relative penalties of statistical microstructures which are inevitable in natural composites and high-throughput manufacturing technologies. In particular, the results show that a hard phase with both high strength (small flaws) and minimal statistical variation in flaw size is key to achieving high crack resistance. This finding is consistent with our simulations of nacre-like composites as well as general failure of brittle materials: for maximum performance the microarchitecture should be as controlled as possible with minimal defects/flaws (Pro et al., 2015a; Abid et al., 2019). Overall the mechanisms identified in the DEM simulations are consistent with those observed in experiments of natural enamel including crack deflection and branching/bifurcation (Bajaj and Arola, 2009a; Yahyazadehfar et al., 2013; Bajaj and Arola, 2009b, Bajaj et al., 2010). The general findings and main mechanisms are summarized below:

(1) Decussation amplifies the overall crack resistance and promotes spread of the inelastic region. The emergent crack path forms a sawtooth waveform in the plies with a frequency that matches the frequency of the periodic microstructure for moderate strength contrast ($\frac{\sigma_{ru}}{\sigma_0} = 21.4$).
(2) Stronger rods generate higher crack resistance and for large enough strength contrast (e.g., $\sigma_{ru} = 28.5$, $E_r/kd = 10$, $\theta_D = 30^0$), higher frequencies are introduced into the crack path due to intense pinning of the crack at the crisscrossing points between adjacent rods. Weak rods (e.g., $\sigma_{ru} = 7.1$, $E_r/kd = 10$, $\theta_D = 30^0$) tended to break symmetry in the material and form a full kinked crack with daughter cracks which reduced overall crack resistance.
(3) Stiffer rods decrease the crack resistance (fixed decussation and strength). For high stiffness contrast the rod stresses are amplified and fracture before the interface process zone can develop at a rate fast enough to offset the negative effect of rod fracture, leading to a net decrease in the overall crack resistance.
(4) Spatial variations in rod strength always decreased the overall toughness. For low coefficients of variation in rod strength ($\Delta\sigma_{ru}/\bar{\sigma}_{ru} < 0.5$) the crack resistance was relatively unaffected but as higher coefficients of variation were introduced the probability of daughter cracks being formed increased. For large coefficients of variation ($\Delta\sigma_{ru}/\bar{\sigma}_{ru} = 0.3$) daughter cracks were formed in much greater numbers at larger length scales from the main crack line. Daughter cracks caused local oscillations in $\frac{R}{\Gamma_i}$ and ultimately reduced the average toughness. Local oscillations in the crack path were associated with local oscillations in $\frac{R}{\Gamma_i}$ which varied from one realization to the next, but the average process zone distribution remained relatively constant.

The results in this study are an extension of our previous models (Pro and Barthelat, 2019), and in addition to offering a better understanding of the mechanics of natural enamel, they can be incorporated into the design of restorative dental materials as well as serve as basic guidelines for tough bioinspired crossplies. The explicit DEM approach is general and can be used to model complex fracture in other types of composites such as Bouligand structures (already in progress), synthetic laminated composites, and multilayered coating systems (e.g., thermal and environmental barrier coatings). The same explicit DEM approach could also be used to study dynamic impact and fracture in architectured glass inspired from our previous experiments (Yin et al., 2018; Yin et al., 2019b). In general the explicit DEM algorithm offers a robust approach for obtaining numerical solutions involving complex crack propagation, and as shown here can be used to obtain true specimen independent material properties. Coupled with broad parametric studies and/or machine learning algorithms, this powerful approach could aid to understand and expand the general structure-property space for modern composites.

Declaration of Competing Interest

The authors declare that they have no known competing financial interests or personal relationships that could have appeared to influence the work reported in this paper.

CRediT authorship contribution statement

J. William Pro: Conceptualization, Methodology, Software, Validation, Formal analysis, Investigation, Writing - original draft, Visualization. **Francois Barthelat:** Conceptualization, Methodology, Investigation, Resources, Writing - review & editing, Supervision, Project administration, Funding acquisition.

Acknowledgments

This research was funded by a strategic grant (STPGP 479137-15) from the Natural Sciences and Engineering Research Council of Canada (NSERC) and by a team grant (191270) from the Fonds de Recherche du Quebec – Nature et Technologies. Computations were made on the supercomputers Graham and Cedar at University of Waterloo and Simon Fraser University respectively, managed by Compute Canada. The operation of these supercomputers is funded by the Canada Foundation for Innovation (CFI).

References

Abid, N., Pro, J.W., Barthelat, F., 2019. Fracture mechanics of nacre-like materials using discrete-element models: effects of microstructure, interfaces and randomness. J. Mech. Phys. Solids 124, 350–365.

Ahrens, J., Geveci, B., Law, C., 2005. Paraview: an end-user tool for large data visualization. In: The Visualization Handbook, p. 717.

Anderson, T.L., 2017. Fracture Mechanics: Fundamentals and Applications. CRC press.

Ashby, M.F., Cebon, D., 1993. Materials selection in mechanical design. Le J. Phys. IV 3 (C7) C7–1-C7-9.

Bažant, Z.P., 1984. Size effect in blunt fracture: concrete, rock, metal. J. Eng. Mech. 110 (4), 518–535.

Bažant, Z.P., 2004. Scaling theory for quasibrittle structural failure. In: Proceedings of the National Academy of Sciences, 101, pp. 13400–13407.

Bajaj, D., Arola, D.D. , 2009a. On the R-curve behavior of human tooth enamel. Biomaterials 30 (23–24), 4037–4046.

Bajaj, D., Arola, D. , 2009b. Role of prism decussation on fatigue crack growth and fracture of human enamel. Acta Biomater. 5 (8), 3045–3056.

Bajaj, D., Park, S., Quinn, G.D., Arola, D., 2010. Fracture processes and mechanisms of crack growth resistance in human enamel. JOM 62 (7), 76–82.

Barani, A., Bush, M.B., Lawn, B.R., 2012. Effect of property gradients on enamel fracture in human molar teeth. J. Mech. Behav. Biomed. Mater. 15, 121–130.

Barthelat, F., Rabiei, R., 2011. Toughness amplification in natural composites. J. Mech. Phys. Solids 59 (4), 829–840.

Barthelat, F., 2015. Architectured materials in engineering and biology: fabrication, structure, mechanics and performance. Int. Mater. Rev. 60 (8), 413–430.

Bechtle, S., Habelitz, S., Klocke, A., Fett, T., Schneider, G.A., 2010. The fracture behaviour of dental enamel. Biomaterials 31 (2), 375–384.

Boyde, A., 1989. Enamel, Teeth. Springer, pp. 309–473.

Cook, R.D., Malkus, D.S., Plesha, M.E., 1974. Concepts and Applications of Finite Element Analysis. Wiley New York.

Cox, B., 2010. A multi-scale, discrete-cell simulation of organogenesis: application to the effects of strain stimulus on collective cell behavior during ameloblast migration. J. Theor. Biol. 262 (1), 58–72.

Cox, B.N., 2013. How the tooth got its stripes: patterning via strain-cued motility. J. R. Soc. Interface 10 (84), 20130266.

Cuy, J.L., Mann, A.B., Livi, K.J., Teaford, M.F., Weihs, T.P., 2002. Nanoindentation mapping of the mechanical properties of human molar tooth enamel. Arch. Oral Biol. 47 (4), 281–291.

Danzer, R., 1992. A general strength distribution function for brittle materials. J. Eur. Ceram. Soc. 10 (6), 461–472.

Davis, T.A., 1993. User's Guide For the Unsymmetric-Pattern Multifrontal Package (UMFPACK), Technical Report TR-93-020, CIS Department. University of Florida Gainesville, FL.

Evans, A., Zok, F., 1994. The physics and mechanics of fibre-reinforced brittle matrix composites. J. Mater. Sci. 29 (15), 3857–3896.

Evans, A.G., Mumm, D., Hutchinson, J., Meier, G., Pettit, F., 2001. Mechanisms controlling the durability of thermal barrier coatings. Prog. Mater Sci. 46 (5), 505–553.

Evans, A., 1991. The mechanical properties of reinforced ceramic, metal and intermetallic matrix composites. Mater. Sci. Eng. A 143 (1–2), 63–76.

Gibson, R.F., 2016. Principles of Composite Material Mechanics. CRC press.

Jiang, H., Liu, X.-Y., Lim, C.T., Hsu, C.Y., 2005. Ordering of self-assembled nanobiominerals in correlation to mechanical properties of hard tissues. Appl. Phys. Lett. 86 (16), 163901.

Khandelwal, A., Kumar, A., Ahluwalia, R., Murali, P., 2017. Crack propagation in staggered structures of biological and biomimetic composites. Comput. Mater. Sci. 126, 238–243.

Lawn, B.R., Lee, J.J.-W., Constantino, P.J., Lucas, P.W., 2009. Predicting failure in mammalian enamel. J. Mech. Behav. Biomed. Mater. 2 (1), 33–42.

Lu, C., Danzer, R., Fischer, F.D., 2002. Fracture statistics of brittle materials: Weibull or normal distribution. Phys. Rev. E 65 (6), 067102.

Maas, M.C., Dumont, E.R., 1999. Built to last: the structure, function, and evolution of primate dental enamel. Evol. Anthropol. Issues News Rev. 8 (4), 133–152.

Needleman, A., Tvergaard, V., 1991. A numerical study of void distribution effects on dynamic, ductile crack growth. Eng. Fract. Mech. 38 (2–3), 157–173.

Park, S., Wang, D.H., Zhang, D., Romberg, E., Arola, D., 2008. Mechanical properties of human enamel as a function of age and location in the tooth. J. Mater. Sci. Mater. Med. 19 (6), 2317–2324.

Parmigiani, J., Thouless, M., 2006. The roles of toughness and cohesive strength on crack deflection at interfaces. J. Mech. Phys. Solids 54 (2), 266–287.

Parmigiani, J., Thouless, M., 2007. The effects of cohesive strength and toughness on mixed-mode delamination of beam-like geometries. Eng. Fract. Mech. 74 (17), 2675–2699.

Paz, M., 1985. Structural Dynamics. Springer.

Press, W.H., Teukolsky, S.A., Vetterling, W.T., Flannery, B.P., 2007. Numerical recipes. The Art of Scientific Computing, 3rd edition Cambridge university press.

Prior, A., 1994. Applications of implicit and explicit finite element techniques to metal forming. J. Mater. Process. Technol. 45 (1–4), 649–656.

Pro, J.W., Barthelat, F., 2019. Discrete element models of tooth enamel, a complex three-dimensional biological composite. Acta Biomater. 94, 536–552.

Pro, J.W., Lim, R.K., Petzold, L.R., Utz, M., Begley, M.R. , 2015a. The impact of stochastic microstructures on the macroscopic fracture properties of brick and mortar composites. Extreme Mech. Lett. 5, 1–9.

Pro, J.W., Lim, R.K., Petzold, L.R., Utz, M., Begley, M.R. , 2015b. GPU-based simulations of fracture in idealized brick and mortar composites. J. Mech. Phys. Solids 80, 68–85.

Pro, J.W., Sehr, S., Lim, R.K., Petzold, L.R., Begley, M.R., 2018. Conditions controlling kink crack nucleation out of, and delamination along, a mixed-mode interface crack. J. Mech. Phys. Solids 121, 480–495.

Rajan, V.P., Zok, F.W., 2014. Matrix cracking of fiber-reinforced ceramic composites in shear. J. Mech. Phys. Solids 73, 3–21.

Sehr, S., Amidi, S., Begley, M.R., 2019. Interface delamination vs. bulk cracking along wavy interfaces. Eng. Fract. Mech. 206, 64–74.

Spears, I., 1997. A three-dimensional finite element model of prismatic enamel: a re-appraisal of the data on the Young's modulus of enamel. J. Dent. Res. 76 (10), 1690–1697.

Srivastava, A., Ponson, L., Osovski, S., Bouchaud, E., Tvergaard, V., Needleman, A., 2014. Effect of inclusion density on ductile fracture toughness and roughness. J. Mech. Phys. Solids 63, 62–79.

Tada, H., Paris, P.C., Irwin, G.R., 1973. The Stress Analysis of cracks, Handbook. Del Research Corporation.

Thouless, M.D., Evans, A.G., 1988. Effects of pull-out on the mechanical properties of ceramic-matrix composites. Acta Metall. 36 (3), 517–522.

Xu, X.-P., Needleman, A., 1994. Numerical simulations of fast crack growth in brittle solids. J. Mech. Phys. Solids 42 (9), 1397–1434.

Yahyazadehfar, M., Arola, D., 2015. The role of organic proteins on the crack growth resistance of human enamel. Acta Biomater. 19, 33–45.

Yahyazadehfar, M., Bajaj, D., Arola, D.D., 2013. Hidden contributions of the enamel rods on the fracture resistance of human teeth. Acta Biomater. 9 (1), 4806–4814.

Yin, Z., Dastjerdi, A., Barthelat, F., 2018. Tough and deformable glasses with bioinspired cross-ply architectures. Acta Biomater. 75, 439–450.

Yin, S., Yang, W., Kwon, J., Wat, A., Meyers, M.A., Ritchie, R.O. , 2019a. Hyperelastic phase-field fracture mechanics modeling of the toughening induced by Bouligand structures in natural materials. J. Mech. Phys. Solids.

Yin, Z., Hannard, F., Barthelat, F. , 2019b. Impact-resistant nacre-like transparent materials. Science 364 (6447), 1260–1263.

Zhou, F., Molinari, J.-F., 2004. Stochastic fracture of ceramics under dynamic tensile loading. Int. J. Solids Struct. 41 (22–23), 6573–6596.